Direct Differentiation of Pathological Changes in the Human Lung Parenchyma With Grating-Based Spectral X-ray Dark-Field Radiography

Kirsten Taphorn, Korbinian Mechlem, Thorsten Sellerer, Fabio De Marco, Manuel Viermetz, Franz Pfeiffer, Daniela Pfeiffer, and Julia Herzen

Abstract—Diagnostic lung imaging is often associated with high radiation dose and lacks sensitivity, especially for diagnosing early stages of structural lung diseases. Therefore, diagnostic imaging methods are required which provide sound diagnosis of lung diseases with a high sensitivity as well as low patient dose. In small animal experiments, the sensitivity of grating-based X-ray dark-field imaging to structural changes in the lung tissue was demonstrated. The energy-dependence of the X-ray dark-field signal of lung tissue is a function of its microstructure and not yet known. Furthermore, conventional X-ray dark-field imaging is not capable of differentiating different types of pathological changes, such as fibrosis and emphysema. Here we demonstrate the potential diagnostic power of grating-based X-ray dark-field in combination with spectral imaging in human chest radiography for the direct differentiation of lung diseases. We investigated the energy-dependent linear diffusion coefficient of simulated lung tissue with different diseases in wave-propagation simulations and validated the results with analytical calculations. Additionally, we modeled spectral X-ray dark-field chest radiography scans to exploit these differences in energy-dependency. The results demonstrate the potential to directly differentiate structural changes in the human lung. Consequently, grating-based spectral X-ray dark-field imaging potentially contributes to the differential diagnosis of structural lung diseases at a clinically relevant dose level.

Index Terms—Imaging modalities, lung, x-ray imaging and computed tomography.

I. Introduction

STRUCTURAL lung diseases change the microstructure of the human lung parenchyma and increase the risk of developing critical health conditions. Therefore, their diagnosis is particularly important in the early stages of disease development. By that, the chances of recovery increase and the mortality rate is lower [1]. For this purpose, a variety of examination methods are established in clinical routine. The most commonly used tools are diagnostic imaging modalities such as chest radiography, computed tomography (CT) or magnetic resonance imaging (MRI). Chest radiography is usually the first exploratory examination as it is fast, inexpensive and universally available. Due to the weak absorption of the lung tissue compared to the surrounding thorax, the method lacks sensitivity, especially in the early detection of lung diseases. The effective dose in conventional thoracic radiography is low, with up to 0.04 mSv. CT is superior in terms of high resolution and sensitivity. In addition, it provides three-dimensional information about the body's internal structure, which allows the quantification of lung diseases and their detection in early stages. However, in routine examinations a high patient dose of approximately 7 mSv is applied [2]. MRI is not based on ionizing radiation, but its accessibility is limited and examinations are time consuming and costly [3]. Consequently, there is a high demand for a low-dose diagnostic imaging modality with a high sensitivity for early structural lung changes, that is additionally time- and cost-efficient.

In recent years, spectral X-ray imaging was further developed. Measurements of the sample with at least two photon spectra are required to exploit the differences in the energy-dependent behavior of materials and to gain more information about the sample. Different technical implementations, such as dual-source CT, dual-layer detector systems or rapid kVp-switching devices, are currently used [4]. Recent advances in technology include photon-counting detectors, which are capable of acquiring multiple, spatially and temporally co-registered energy-resolved images with a single acquisition [5]. Dual-energy CT provides material-specific information, which has been shown to be beneficial for diagnostics in clinical applications [6], [7]. In addition, spectral X-ray imaging enables the quantification of the effective atomic number [4], and the suppression of beam-hardening artifacts additionally increases the image quality [8].

Of particular interest for diagnostic lung imaging is grating-based X-ray dark-field imaging (XDF) with a Talbot-Lau interferometer. This method is sensitive to structural features below the pixel size (e.g., alveoli in chest radiographs) and is based on small-angle X-ray scattering [9]. In small animal disease models, the diagnostic power of XDF imaging was demonstrated with table-top experiments for various lung diseases such as emphysema [10], [11] and fibrosis [12]. Both lung diseases lead to a decrease in dark-field signal compared to that of healthy lung tissue. The feasibility of a Talbot-Lau interferometer for XDF imaging of pigs [13] and human bodies [14] in situ was demonstrated using a fringe scanning approach.

A limitation of XDF imaging is the direct differentiation of pathological changes in the lung, since they are all associated with a decrease in the dark-field signal. In the specific problem case of combined pulmonary fibrosis and emphysema syndrome (CPFE), fibrotic lung tissue, which is typically expressed in the lower lobes of the lung [15], might not be distinguished from emphysematous tissue in XDF imaging.

By combining spectral and XDF imaging to take advantage of the energy-dependent scattering properties of the sample, additional information about its subpixel microstructure can be accessed. A recent study demonstrated that the energy-dependence of the dark-field signal varies for materials with different microstructures. This information can be used to differentiate the materials [16]. Compared to the energy-dependency of the attenuation signal, however, the energy-dependent behavior of the dark-field signal is not only material-specific but also depends on the imaging setup. The dark-field signal is additionally influenced by polychromatic effects such as beam-hardening [17], [18] and visibility hardening [19], which are highly relevant for clinical applications.

In this work, we investigate the advantages of spectral XDF imaging for clinical applications. With wave-optical simulations of a Talbot-Lau interferometer, the energy-dependent dark-field signal of different lung pathologies was determined. This information was then used as input for the calculation of dark-field images of the FORBILD thorax phantom [20] based on projection integrals. The results demonstrate the ability
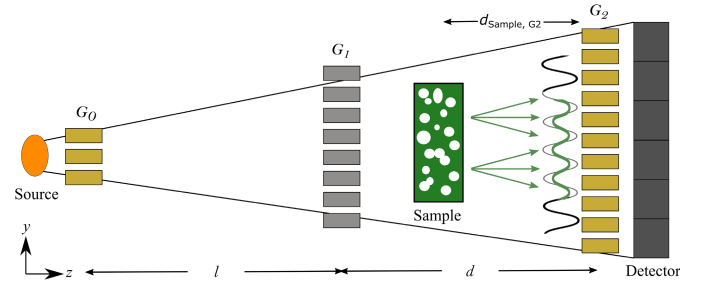

Fig. 1. Three-grating Talbot-Lau interferometer with a scattering sample. The reference grating G_1 is positioned at a distance l behind the source grating G_0 and creates an intensity modulation in front of the analyzer grating G_2, which is at a distance d to G_1. The scattering sample reduces the visibility of the intensity pattern (compare green and gray intensity pattern). The detector is positioned behind G_2.

to distinguish between different lung diseases at a clinically relevant dose level with spectral XDF imaging.

II. MATERIALS AND METHODS

A. Grating-Based Spectral X-ray Dark-Field Imaging

Contrary to most other X-ray phase-contrast imaging techniques, XDF imaging with a Talbot-Lau interferometer is feasible with polychromatic incoherent sources and large-pixel detectors, and thus suitable for clinical applications [21]. A sketch of a Talbot-Lau interferometer is depicted in Fig. 1. The interferometer consists of three diffraction gratings. The strongly absorbing source grating G_0 provides a set of spatially coherent wavefronts [21]. The reference grating G_1 creates an intensity modulation with high spatial frequency at a certain distance, where the analyzer grating G_2 is positioned, so that it converts the high frequency modulations into a low-frequency pattern.

A sample in the beam path leads to a change in the intensity modulation. This is shown as an example of a purely scattering object in Fig. 1. Small-angle X-ray scattering blurs the intensity modulation and reduces the visibility of the fringe pattern compared to a sample-free measurement (cf. green and gray intensity modulation in Fig. 1, respectively).

The attenuation and refraction properties of an object are described by the material-specific refractive index,

$$n = 1 - \delta + i\beta = 1 - \frac{2\pi \rho_e r_e}{k^2} + i\frac{\mu}{2k}, \tag{1}$$

where ρ_e is the electron density, μ is the absorption coefficient, r_e the classical electron radius and the wave number is $k = 2\pi/\lambda$. When passing through the sample with refractive index n, a plane wave with wave vector $\mathbf{k}$ at the position $\mathbf{r}$ is described by [22]

$$\Psi(\mathbf{r}) = \Psi_0 \exp(i\mathbf{kr}) \cdot \exp(-i\delta\mathbf{kr}) \cdot \exp(-\beta\mathbf{kr}). \tag{2}$$

In vacuum, the field propagates as $\Psi = \Psi_0 \exp(i\mathbf{kr})$. The factor $\exp(-i\delta\mathbf{kr})$ is related to a shift in phase and $\exp(-\beta\mathbf{kr})$ describes the decay of intensity due to absorption [23].

The correlation length $\xi_{corr}(E)$ of the interferometer describes the length scale on which correlations of the projected electron density within the sample can be probed and

is related to the sensitivity S and the energy E of the X-ray beam [24],

$$\xi_{\text{corr}}(E) = S \cdot \frac{hc}{E}. \tag{3}$$

Planck's constant is denoted with h and c is the speed of light. The sensitivity S of a Talbot-Lau interferometric setup is defined by,

$$S = \begin{cases} \dfrac{d_{\text{Sample},G2}}{p_{G2}}, & \text{Sample between } G_1 \text{ and } G_2, \\ \dfrac{d_{G0,\text{Sample}}}{p_{G0}}, & \text{Sample between } G_0 \text{ and } G_1, \end{cases} \tag{4}$$

with p being the period of the analyzer or source grating and d the distance between the sample and analyzer grating or source grating, depending on whether the sample is between G_0 and G_1 or G_1 and G_0, respectively.

The image data is acquired with a phase-stepping. One grating is moved perpendicularly to the beam in equidistant steps and the intensity is recorded. The stepping curve obtained gives the intensity based on the relative stepping position of the moved grating. The attenuation, phase-contrast and dark-field signals can be extracted from this stepping curve.

Similarly to the absorption coefficient $\mu(E)$, the linear diffusion coefficient $\varepsilon(E)$ is defined for the dark-field channel and is energy-dependent. The dark-field signal $-\ln(D(E))$ of a macroscopically homogeneous sample is given as [25]

$$-\ln(D(E)) = \varepsilon(E) \cdot d = \sigma(E) \cdot (1 - G(\xi_{\text{corr}}(E))) \cdot d. \tag{5}$$

The dark-field signal increases with the sample thickness d. The linear diffusion coefficient $\varepsilon(E)$ is given by the projected autocorrelation function G of ρ_e, at the length scale of the correlation length $\xi_{\text{corr}}(E)$ [24]. The scattering cross section $\sigma(E)$ as well as the projected autocorrelation function $G(\xi_{\text{corr}}(E))$ are energy-dependent [26] and material-specific quantities. According to Andersson $et~al.$ [27], the autocorrelation function of a two-dimensional electron density distribution $\rho(y,z)$ is defined as,

$$\gamma(y',z') = \frac{\int\int \Delta\rho(y,z)\Delta\rho(y+y',z+z')dydz}{\int\int \Delta\rho(y,z)\Delta\rho(y,z)dydz}. \tag{6}$$

The coordinate system is consistent with Fig. 1. The fluctuations in electron density around the mean electron density $\overline{\rho(y,z)}$ are

$$\Delta\rho(y,z) = \rho(y,z) - \overline{\rho(y,z)}, \tag{7}$$

and the central peak of the autocorrelation function is normalized to unity. The same applies to the three-dimensional case. XDF imaging with a grating interferometer is sensitive to scattering only perpendicular to the grating lamellae and the beam direction (cf. y-direction in Fig. 1). Therefore, the projected autocorrelation function G is calculated by

$$G(\xi_{\text{corr}}) = \frac{\int \gamma(y' = \xi_{\text{corr}}, z')dz'}{\int \gamma(y' = 0, z')dz'}. \tag{8}$$

B. Wave-Propagation Simulations and Analytical Calculations

1) Sample and Setup: With wave-propagation simulations, the energy-dependent dark-field signal for healthy lung, fibrotic and emphysematous tissue were determined. The lung parenchyma for pulmonary fibrosis, pulmonary emphysema and healthy lung tissue were based on simulated 2D Voronoi grids. A Voronoi grid is a decomposition of an area into cells, where a cell is defined as the nearest area around a center point [28]. Voronoi grids are visually very similar to the human lung parenchyma and their structural parameters can be easily controlled. Furthermore, 3D-printed Voronoi grids were recently introduced as phantom materials for lung tissue [29], [30].

We used 10 samples per pathology to determine the mean dark-field signal with a Talbot-Lau interferometer. The size of each lung parenchyma sample was $0.9\,\text{cm} \times 0.9\,\text{cm}$. Each 2D lung parenchyma sample was created separately and did not represent sections of a 3D model of the human lung. The sampling could be chosen individually. The number of center points per cm^2 for the different pathologies was varied in order to obtain realistic alveolar sizes. The mean alveolar density in the human lung base has been reported as 21.2 alveoli per mm^3 and increases toward the lung apex [31]. If a simple cubic arrangement of spherical alveoli is assumed, the number of alveoli in $0.9\,\text{cm} \times 0.9\,\text{cm}$ is 620 with a packing fraction of $p_{\text{sc}} = \pi/6$. The Voronoi grids intrinsically have a packing fraction of $p_{\text{v}} = 1$, which results in approximately 1186 cells in the Voronoi-based parenchyma sample. The number of cells for the lung parechnyma phantom of healthy lung was varied between 1250 and 1450 to account for the increased alveolar density toward the lung apex.

To simulate fibrotic lung parenchyma, 42 to 58 iterations of binary dilation [32] were applied to the healthy lung parenchyma samples to account for the formation of excess tissue and the densification of alveoli related to fibrosis.

Emphysema is associated with the destruction of the alveolar walls and is common in patients with chronic obstructive pulmonary disease [33]. For emphysematous lung parenchyma, we reduced the number of cells to values between 250 and 320.

The measured mean chord length (MCL) ensured realistic alveolar sizes. The MCL is a medically-approved measure for determining the size of human alveoli in histological analysis, which is known to vary for different lung diseases. We used the direct approach [34] to measure the MCL, with a set of 600 random test lines in both horizontal and vertical direction. In addition to the MCL, the approach provides the mean wall thickness (MWT) of lung alveoli.

Table I shows the specifications of the simulated setup. The G_0 and G_2 gratings consisted of gold with a height of 200 μm, a period of 11.6 μm, and a duty cycle of 0.5. The G_1 was a $\pi/2$-phase shifting grating consisting of nickel with a height of 7.7 μm. The parameters were chosen so that a Talbot distance of 1.2 m for the design energy of 44 keV was achieved. The sample position was between G_1 and G_2 at a distance of 30 cm behind G_1. The corresponding sensitivity was $S = 7.76 \cdot 10^4$,

GEOMETRY AND GRATING SPECIFICATIONS OF THE SIMULATION SETUP. THE PARAMETERS OF THE SIMULATED TALBOT-LAU INTERFEROMETER ARE ACCORDING TO THE SKETCH IN FIG. 1

Pixel size [µm]	$l = d$ [cm]	d_{Sample,G_2} [cm]	Magnification
500	120	90	1.61

	Period [µm]	Material / Height [µm]	Duty cycle
G_0	11.6	Gold / 200	0.5
G_1	5.8	Nickel / 7.7	0.5
G_2	11.6	Gold / 200	0.5

according to eq. (4). The pixel size was 500 µm and due to the magnification of 1.61, the effective pixel size was 311 µm. The electron density ρ_e as well as the absorption coefficient $\mu(E)$ for lung tissue were taken from the XMuDat database [35], which is based on calculations by Boone and Chavez [36].

2) Simulation of Image Data: The dark-field signal for monochromatic X-rays ranging from 30 keV to 100 keV with a step size of 1 keV was simulated. The assumed wavefront was sampled in 0.046 µm steps in order to represent propagation effects with sufficient resolution.

We used a wave-optical simulation package with an implementation of free-space propagation and a rescaling of the cone-beam propagation distances according to the Fresnel scaling theorem [22]. As the phantoms were only two-dimensional (extending in the y-z plane) and the X-ray source was incoherent in the direction parallel to the grating bars, only a one-dimensional section of the wavefront ($x = 0$) was propagated. This reduces the required memory as well as the computational complexity [37]. Furthermore, we used the multi-slice projection approximation. Especially if the sample extension in beam direction is large compared to the propagation distance of the wavefront, propagation effects throughout the sample cannot be neglected and are correctly modeled with the multi-slice projection approximation [38].

The sample was divided into adjacent slices perpendicular to the propagation direction (400 slices in our simulation resulting in a sample thickness of 2.25 µm per slice), which were considered as a series of equidistant lines. The wavefront was propagated to the first projected sample line and the interaction of $\Psi(\mathbf{r})$ with the projected sample line with refractive index n, according to eq. (1), was calculated with eq. (2). The wavefront was propagated to the next sample line and $\Psi(\mathbf{r})$ was updated.

The gratings were applied to the wavefront. By a convolution of the propagated intensity with the G_0 slot profile, the source was assumed to be incoherent. The stepping curve was sampled at five different grating positions of G_2, which were evenly distributed over one grating period.

3) Analytical Calculations: For the analytical calculation of the linear diffusion coefficient, we calculated the projected autocorrelation function with eq. (6), (7) and (8) for the same samples used in the wave-propagation simulation. We averaged $G(\xi_{\mathrm{corr}})$ over multiple angles for each lung parenchyma phantom to increase the statistics. This is possible because of the isotropy of the samples.

4) Data Analysis: We fitted the energy-dependent dark-field signals of the individual samples for both wave-propagation

simulation and analytical calculations with a power law,

$$f(E) = a \cdot E^{-b}, \tag{9}$$

to extract the signal strength a and the energy-exponent b. We normalized the dark-field signal from the wave-propagation simulation to the thickness of the sample in beam direction prior to the fit. The energy range was 30 to 100 keV in both, simulation and analytical calculation.

Considering the case of packed hollow microspheres with far smaller radii than the correlation length of the setup, the projected autocorrelation function $G(\xi_{\mathrm{corr}}(E))$ approaches zero. Thus, the energy-dependency of the linear diffusion coefficient in eq. (5) is given by the scattering cross section with $\varepsilon(E) \propto E^{-2}$. For larger radii compared to the correlation length, $G(\xi_{\mathrm{corr}}(E))$ is not constant and consequently the energy-dependency varies up to $\varepsilon(E) \propto E^{-4}$ [39]. Thus, the energy-dependency of the lung parenchyma is expected to be in a range of E^{-2} to E^{-4}.

C. Forward-Model-Based Spectral X-ray Dark-Field Radiography

The spectral grating-based XDF projections of the FORBILD thorax phantom [20] were calculated based on the spectral grating-based imaging model. Mechlem *et al.* [40] introduced the model first and demonstrated that it correctly describes spectral grating-based phase-contrast and dark-field imaging with the projection approximation, which neglects the extent of the sample in the beam direction. The spectral grating-based imaging model gives the number of counts y_i^{rs} in pixel i for stepping position r in the energy bin s and a homogeneous sample by

$$y_i^{rs} = \int_{-\infty}^{\infty} \Phi(E) R^s(E) e^{-\int \mu_i(E) dz}$$
$$\times \left[1 + V(E) e^{-\int \varepsilon_i(E) dz} \cdot \cos(\phi^r(E) + \Delta\phi_i(E)) \right] dE. \tag{10}$$

The reference phase at phase step r is denoted with $\phi^r(E)$ and the phase shift by the sample is given by $\Delta\phi(E)$, $\Phi(E)$ is the source spectrum and $R^s(E)$ gives the response function of the photon-counting detector. The beam path is assumed to be in z-direction.

1) Setup and Sample: The setup geometry of the wave-optical simulations (Table I) was used. The acceleration voltage was 120 kVp. A thick aluminum filter (7.0 mm) was chosen in order to reduce beam-hardening artifacts. The detector was a 1400×1400 pixels photon-counting detector with a cadmium telluride sensor layer, an active area of 70 cm × 70 cm and a sensor thickness of 300 µm. The detector response functions $R^s(E)$ as described by Schlomka *et al.* [41] were used, which account for distortion effects like charge-sharing or K-escapes.

The effective spectra $\Phi(E) R^s(E)$ of the low and high energy bin are depicted in Fig. 2 in blue and orange, respectively. Additionally, the visibility spectrum $V(E)$ of the Talbot-Lau interometer is plotted in red. The first visibility peak is at the design energy of 44 keV. A setup with a
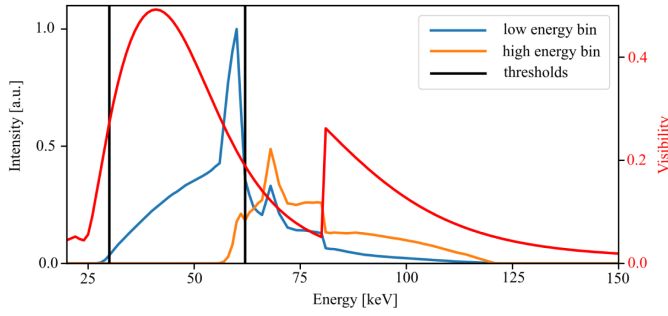
Fig. 2. Effective spectra of the low (blue) and high energy bin (orange) and visibility spectrum (red) of the simulated Talbot-Lau interferometer. The threshold positions are depicted in black.

$\pi/2$ phase-shifting grating has advantages for spectral XDF imaging because the visibility spectrum features a second peak at twice the design energy [42] (at 88 keV). The chosen thresholds were at 30 keV and 62 keV in order to exploit the maxima in the source spectrum as well as the visibility spectrum. The threshold settings are indicated as vertical black lines in Fig. 2. We assumed the phantom to be 30 cm behind G_1, between G_1 and G_2.

The FORBILD thorax phantom consisted of bone, soft-tissue, and lung tissue and was imaged in posterior-anterior position. The coronal chest diameter was 35 cm. We calculated spectral XDF radiographs for two different phantom cases. First, a phantom with healthy lungs served as a reference. The second case was CPFE, with fibrosis expressed in the lower lobes and emphysematous tissue in the upper lobes. Pathological changes were inserted in the lung by replacing spherical regions with a diameter of 3.22 cm of healthy lung tissue with fibrotic or emphysematous tissue.

2) Calculation of Image Data: The radiographs were calculated based on the projection approximation and the phantom was modeled as a 2D plane. The attenuation coefficients and electron densities for the different tissue types were taken from the XMuDat database [35].

Healthy lung tissue, fibrotic and emphysematous tissue were attributed with the linear diffusion coefficients retrieved from the aforementioned wave-propagation simulations. The linear diffusion coefficients for bone and soft tissue were $\varepsilon(E) = 0$. The overall linear diffusion coefficient was calculated as the sum over the different materials m with the corresponding linear diffusion coefficients $\varepsilon_m(E)$, the volume fraction f_{ε_j} of the material in voxel j and a_{ij} which gives the contribution of voxel j to source-detector ray i,

$$\int \varepsilon_i(E)dz = \sum_m \sum_j a_{ij} f_{\varepsilon_j} \varepsilon_m(E). \qquad (11)$$

The counts in each detector pixel were calculated with eq. (10) with $r = 5$ phase steps. The added Poisson noise accounted for realistic photon noise.

3) Data Analysis: Each contrast channel provides two images, one per energy bin. To differentiate the lung pathologies, we exploited the difference in energy-dependency of the linear diffusion coefficient. In the monochromatic case, where the energy-dependent visibility is not important, the dark-field

signal of a homogeneous material x is

$$-\ln(D(E)) = \varepsilon_x(E) \cdot d_x, \qquad (12)$$

where E is the X-ray energy. The expected value for the signal ratio q_{ev} of $-\ln(D(E))$ in the low and high energy bin image with energies E_l and E_h, respectively, can be simplified to

$$q_{ev} = \frac{-\ln(D(E_l))}{-\ln(D(E_h))} = \frac{\varepsilon_x(E_l) \cdot d_x}{\varepsilon_x(E_h) \cdot d_x} = \left(\frac{E_h}{E_l}\right)^b. \qquad (13)$$

Consequently, the signal ratio q increases for increasing energy-exponent b.

We calculated the signal ratio q_{meas} and applied a Gaussian filter ($\sigma = 1$ pixel). In the realistic case, polychromatic effects have an impact on the signal ratio q. Comparable to beam-hardening in the attenuation channel, visibility hardening occurs in the dark-field channel, mainly in the low energy bin [19]. Consequently, the signal in the low energy bin is underestimated and q decreases as the sample thickness increases. We corrected for visibility hardening by estimating the overall projected lung thickness d for each pixel with eq. (5), the high energy bin dark-field signal $-\ln(D_h)$ and the effective energy in the high bin E_h of the healthy case,

$$d = \frac{-\ln(D_h)}{\varepsilon_{\text{healthy lung}}(E_h)}. \qquad (14)$$

By calculating the dark-signal of a sample only consisting of healthy lung tissue with varying thickness, the difference Δq between the measured and the expected signal ratio, q_{meas} and q_{ev} respectively, was estimated for different thicknesses of lung tissue. The expected signal ratio q_{ev} was calculated with eq. (13) and the mean energy of low and high energy spectrum, $E_l = 43.5$ keV and $E_h = 72.0$ keV, respectively. The corrected signal ratio q_{cor} is given by

$$q_{cor} = q_{meas} + \Delta q(d). \qquad (15)$$

We used the estimated lung thickness for each pixel from the healthy phantom to correct the diseased case as well. From the dark-field signal including lung diseases, it is not possible to calculate the overall lung thickness with eq. (14). However, as the simulated phantom cases have the same morphology, size and position, the overall lung thickness in each pixel does not vary between the different cases.

4) Dose Considerations: The air kerma (kinetic energy released per unit mass) is defined as the sum of the kinetic energy of all charged particles liberated per unit mass of air. It is calculated from the distribution of the uncharged energy fluence with respect to its energy $\Phi(E) \cdot E$, and the mass energy absorption coefficient of air $\left(\frac{\mu_{en}(E)}{\rho}\right)_{air}$ [43],

$$K_{air} = \int \Phi(E) \cdot E \cdot \left(\frac{\mu_{en}(E)}{\rho}\right)_{air} dE. \qquad (16)$$

The absorption coefficient was taken from the XMuDat database. The photon counts per energy bin were normalized to the squared effective pixel size p_{eff}^2. The total air kerma at the phantom's surface facing the source was 0.43 mGy.

The air kerma is dependent on the measurement position whereas the air kerma area product (KAP) is a
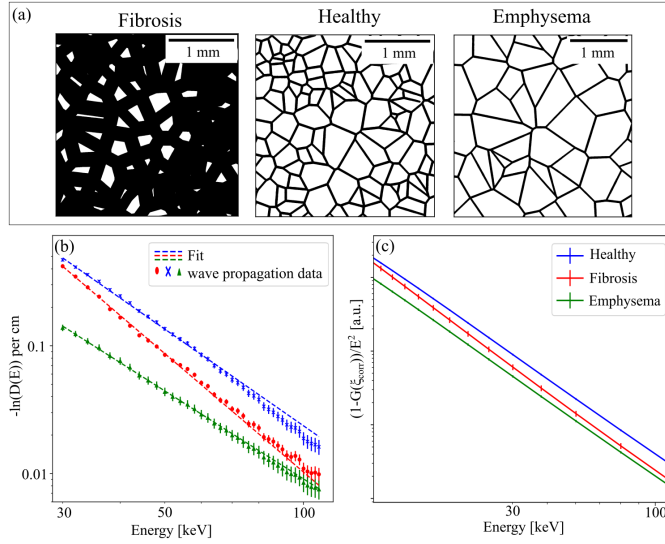
Fig. 3. (a) Simulated lung parenchyma of pulmonary fibrosis, healthy lung and pulmonary emphysema. (b) The energy-dependent mean dark-field signal $-\ln(D(E))$ per cm retrieved from wave-propagation simulations of the setup given in Table I is plotted in double logarithmic representation. The slope varies for different pathologies. The error is given as by the standard deviation. The analytical calculation of $(1 - G(\xi_{corr}))/E^2$ (cf. eq. 5) is depicted in (c) in double logarithmic representation and agrees well with the results from the wave-propagation simulation in (b).

TABLE II

MEAN CHORD LENGTH AND MEAN WALL THICKNESS OF SIMULATED LUNG PARENCHYMA. THE SIGNAL STRENGTH a_{WP} AND ENERGY-EXPONENT b_{WP} WERE RETRIEVED FROM THE FIT OF EQ.(9) AND THE WAVE-PROPAGATION SIMULATIONS. THE RESULTS AGREE WELL WITH THE ANALYTICALLY CALCULATED ENERGY-DEPENDENCY b_{ANA} BASED ON THE PROJECTED AUTOCORRELATION FUNCTION

	Fibrosis	Healthy lung	Emphysema
MCL [μm]	(90.3 ± 5.4)	(209.5 ± 3.6)	(458.6 ± 15.2)
MWT [μm]	(652.48 ± 15.90)	(11.40 ± 0.16)	(12.13 ± 0.20)
a_{wp}	(14890 ± 1147)	(4516 ± 203)	(342 ± 18)
b_{wp}	(3.08 ± 0.02)	(2.51 ± 0.02)	(2.29 ± 0.01)
b_{ana}	(3.110 ± 0.035)	(2.218 ± 0.008)	(2.284 ± 0.003)

position-independent quantity. The KAP is the product of air kerma and the field-of-view at the measurement plane,

$$\text{KAP} = K_{air} \cdot A = K_{air} \cdot \left(n_{pixel} \cdot p_{eff}\right)^2 . \tag{17}$$

The calculated KAP was $0.82\,\text{Gy} \cdot \text{cm}^2$, with $n_{pixel} = 1400$ and $p_{eff} = 0.0311\,\text{cm}$.

III. RESULTS

A. Linear Diffusion Coefficient of Lung Tissue

Examples of the lung parenchyma phantoms based on Voronoi grids for fibrosis, healthy lung tissue and emphysema are depicted in Fig. 3 (a). The measured MCLs and MWTs are given in Table II with uncertainties expressed as the standard deviations. The mean MCL of 90.3 μm of fibrosis was smaller compared to the healthy lung tissue with 209.5 μm. The MCL of emphysema was higher at 458.6 μm.

The mean dark-field signal per cm for the different lung pathologies were obtained as shown in Fig. 3 (b) in double

logarithmic representation. The error bars depict the standard deviation among the 10 parenchyma samples per pathology. The dependency of the linear diffusion coefficient on the energy was fitted with eq. (9), yielding the signal strength a_{wp} and energy-dependency b_{wp}. In double logarithmic representation, the exponent b_{wp} is related to the slope of the line plots in Fig. 3 (b). The results from the wave-propagation simulations are provided in Table II with the corresponding standard deviations. We found that an increase in MWT is related to an increase in energy-dependency b and furthermore, a decrease in MCL is related to an increase in signal strength.

According to eq. (5), the energy-dependency of the dark-field signal is determined by the scattering cross section and the projected autocorrelation function of the sample's electron density at the length scale of the correlation length of the setup. In Fig. 3 (c), the dependency of $(1 - G(\xi_{corr}))/E^2$ on E, averaged over ten samples per pathology, is plotted in double logarithmic representation. The curves were shifted vertically to be in the same order of magnitude. The error bars depict the standard deviation. The results for the energy-dependency b_{ana} are given in Table II as the mean of the ten individual samples. The analytical calculation of a is not possible since the scattering cross section of the samples would have to be known exactly. The results from the wave-propagation simulations are in good agreement with the energy-dependency provided by the analytical calculation.

B. Spectral X-ray Dark-Field Radiography of a Thorax Phantom

Case A in Fig. 4 shows the transmission (a) and dark-field image (b) for the healthy phantom, which were calculated from the sum of the low and high energy image data. The conventional transmission image lacks contrast in the lung region. The dark-field image provides a high signal in the lung, which decreases toward the edges because of the decreasing projected lung thickness. The ribs and vertebrae additionally feature a dark-field signal, which is not related to scattering at microstructures, but rather to strong phase shifts at their edges and beam-hardening induced dark-field.

Figure 4 (c) shows the signal ratio q_{meas} of the dark-field signals in the lung region calculated from the low and high energy bin superimposed with the conventional dark-field image (cf. Fig. 4 (b)). Due to visibility hardening, q_{meas} decreases toward the middle of the lung. In Fig. 4 (d), the corrected signal ratio q_{cor} is depicted. The artifacts due to the visibility hardening are reduced and the signal ratio is homogeneous throughout the lung.

The correction of the signal ratio is based on the difference between the expected and measured q. Figure 4 (e) shows $-\ln(D)$ depending on the projected lung thickness d in solid lines, for both the low and high energy bin, in blue and green, respectively. In comparison, the dotted lines represent the expected dark-field signal, $\varepsilon(E) \cdot d$ with $E_l = 43.5\,\text{keV}$ and $E_h = 72.0\,\text{keV}$, as the mean energy of the low and high energy bin, respectively. As a result, the signal ratio plotted in red in Fig. 4 (e), decreases as the sample thickness increases. The expected signal ratio for
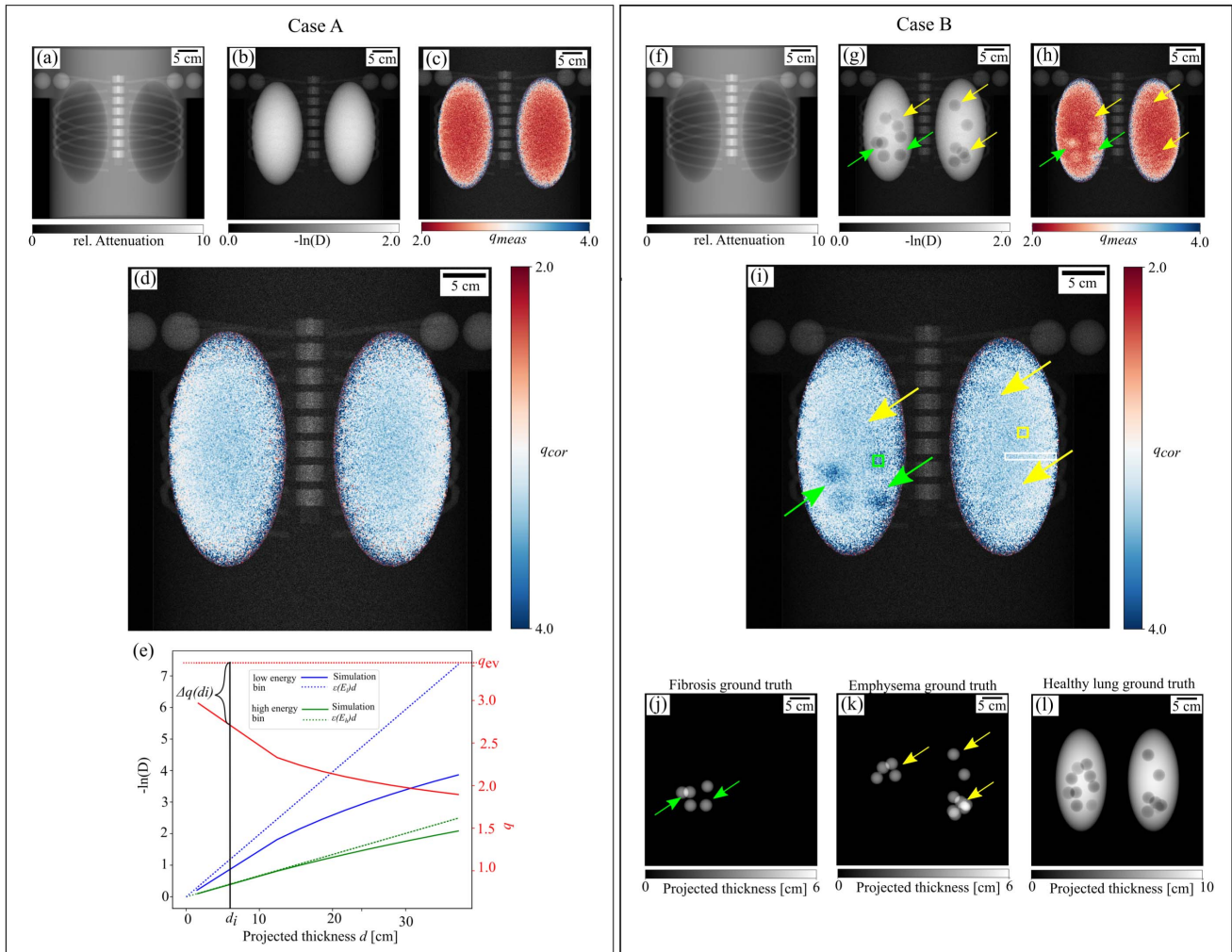
Fig. 4. Spectral X-ray dark-field radiography for two simulated cases. The top row shows the transmission (a,f) and dark-field images (b,g), as well as the overlay of dark-field image and the measured signal ratio q_{meas} (c,h) from the low and high energy bin. Plot (e) shows the impact of visibility hardening on the measured dark-field signal depending on the projected lung thickness, for the low (solid blue line) and high energy bin (solid green line), in comparison to the expected dark-field signal, calculated with $E_l = 43.5$ keV and $E_h = 72.0$ keV, respectively. Furthermore, the behavior of q_{meas} is depicted with a solid red line. For increasing sample thickness, q_{meas} is decreasing and the difference to the expected signal ratio Δq is increasing. The corrected signal ratio q_{cor}, calculated with eq. (15) is depicted in (d) and (i). Case A represents a healthy phantom. Phantom B had CPFE and q_{cor} demonstrates that the reduction of the dark-field signal in the lower right lobe is related to an increased energy-dependency and fibrosis which is in accordance with the ground truth of fibrotic tissue (j). The ground truths for emphysematous and healthy lung tissue are depicted in (k) and (l), respectively.

the healthy lung was at $q_{ev, healthy} = 3.55$, for fibrotic tissue it is increased to $q_{ev, fibrosis} = 4.72$ and emphysema has a similar expected signal ratio compared to healthy lung tissue with $q_{ev, emphysema} = 3.17$. For each projected lung thickness, we estimated Δq to correct the signal ratio. In summary, case A shows how a healthy phantom behaves in spectral XDF imaging.

Case B in Fig. 4 demonstrates the advantages of spectral XDF imaging for the aforementioned problem of CPFE. The transmission image (cf. Fig. 4 (f)) does not provide any contrast in the lung region. But the dark-field image (cf. Fig. 4 (g)) shows reduced signal in small regions spread over the whole lung, which cannot be attributed to a specific lung pathology. The measured and corrected signal ratios are depicted in Fig. 4 (h) and (i), respectively. The healthy lung tissue provides

a homogeneous q_{cor} (cf. the ground truth of projected lung tissue in Fig. 4 (l)). Both the measured and corrected signal ratio show an increased energy-dependency b in the lower regions (cf. green arrows in Fig. 4 (h) and (i)), compared to the healthy lung. According to Table II, these regions are fibrotic tissue, which agrees well with the ground truth of projected fibrotic tissue in Fig. 4 (j). No significant changes are present in the upper lung lobes (cf. yellow arrows in Fig. 4) in q_{cor} and the reduction in the dark-field signal is related to emphysematous tissue, for which the comparison to the emphysema ground truth in Fig. 4 (k) gives evidence.

In Fig. 5 (a), a histogram of the conventional dark-field signal in three regions-of-interest, including healthy lung tissue, emphysema, and fibrosis is shown. The regions are indicated in Fig. 4 (i) with a white, yellow and green box, respectively.
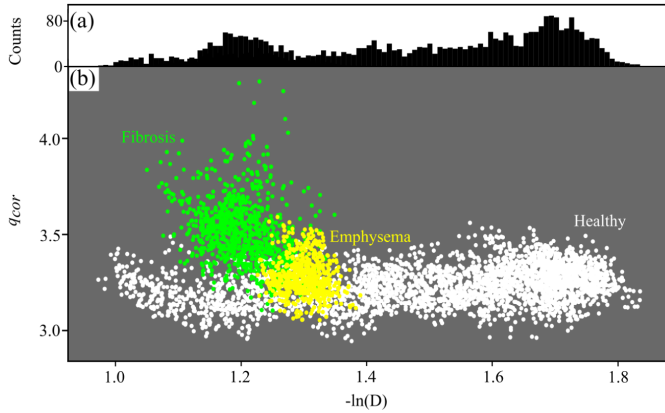
Fig. 5. (a) Histogram of $-\ln(D)$ of small lung regions indicated in Fig. 4 (i). No difference can be distinguished between fibrotic and emphysematous tissue at the smaller peak at $-\ln(D) \approx 1.2$. (b) The scatterplot of the corrected signal ratio q_{cor} of the low and high energy bin depending on the conventional dark-field signal $-\ln(D)$ for the same regions is shown. The healthy lung tissue provides constant q_{cor} values for different $-\ln(D)$. Pixels with fibrotic tissue are better differentiated from healthy and emphysematous tissue compared to the histogram in (a), due to higher q_{cor} for fibrotic tissue compared to healthy lung tissue.

The histogram is widely spread due to a large range of projected lung tissue thicknesses. The first peak at approximately $-\ln(D) \approx 1.2$ is related to the lung diseases (either fibrosis and/or emphysema). The second peak is related to the healthy tissue with high projected thickness. The additional information given by the signal ratio q_{cor} depending on the dark-field signal in Fig. 5 (b) enables the differentiation of the peak at $-\ln(D) \approx 1.2$ into fibrosis and emphysema. The green dots mark pixels with a higher q_{cor} value but a lower overall dark-field signal and are attributed to fibrotic tissue. The yellow dots with a similar q value compared to the healthy lung but similar dark-field signal compared to fibrosis are empyhsematous tissue, which can be distinguished from fibrosis. Healthy lung tissue (cf. white dots in Fig. 5 (b)) provides a constant signal ratio over a range of $-\ln(D)$ values.

IV. DISCUSSION

The parameters of the Voronoi lung parenchyma models for healthy lung, fibrosis and emphysema were selected to reproduce the reference MCL values of human lung tissue. The reported MCL for healthy human lung tissue is 220 μm. Emphysematous lung tissue has an MCL of 500 μm in moderate stages and up to 620 μm in severe cases [44]. Fibrotic tissue has an MCL of approximately 100 μm [45].

The wave-propagation simulations of the energy-dependent dark-field signal show a decreasing signal strength a with increasing MCL and a higher energy-dependence b with increasing MWT. Theoretically, an increasing energy exponent is expected with increasing size of the sample structure (cf. eq.(5)). Consequently, the energy-dependency is possibly determined by the thickness of the alveolar walls. The MWTs of healthy lung and emphysematous tissue were similar and on a length scale closer to the correlation length of the interferometer.

The thorax phantom included moderate emphysema because the diagnosis of early stage lung diseases is of high interest.

In severe emphysema, the destruction of the alveolar walls is more advanced and the MCL is larger. Therefore, a decrease in signal strength a in XDF imaging is expected. However, since the thickness of the alveolar walls is assumed to remain constant, the energy exponent b for severe emphysema is expected to be similar to the moderate case.

The quantitative results for the signal strength and the energy-dependency are only valid for the specific setup parameters used. By assuming that eq. (5) is only a function of the energy according to eq. (9), the spatial extent of the sample in the beam direction is neglected. In reality, the distance between a certain sample point and G_2, $d_{Sample\,G_2}$ is not constant throughout the sample and the projected autocorrelation function $G(\xi_{corr}(E))$ changes for different points within the sample. Consequently, eq. (9) describes the linear diffusion coefficient per unit length as a function of the X-ray energy for a given sensitivity. However, the spatial difference in sensitivity in the lung parenchyma samples was less relevant for extracting the energy-dependency of the dark-field signal in the wave-propagation simulations, since the sample dimensions were much smaller compared to the inter-grating distance.

Furthermore, the linear diffusion coefficient is not an intrinsic property of the material, unlike the attenuation coefficient. It is expected that both the signal strength and the energy-exponent change with the geometry of the setup. In particular, for a fixed energy, the projected autocorrelation function is sampled with a different mean correlation length if the geometry of the setup is changed, and thus the energy-dependency may change.

Figure 4 shows that the signal ratio q of the dark-field signal in low and high energy bin allows a direct differentiation of pulmonary fibrosis and emphysema. This is difficult in conventional chest X-ray and dark-field imaging. Therefore, spectral XDF radiography potentially offers a higher sensitivity for the differentiation of fibrosis and emphysema compared to conventional XDF imaging. In general, the signal ratio depends on the linear diffusion coefficient of the individual scattering materials, which is, among others, given by the sensitivity, more precisely by the setup geometry and the sample position. Higher sensitivities result in a larger correlation length compared to the microstructure size of the sample, and the projected autocorrelation function approaches $G(\xi_{corr}) = 0$ (for $\xi_{corr} \to \infty$). The energy-dependency of the dark-field signal is then entirely given by the scattering cross section ($\propto E^{-2}$) and therefore becomes independent of the microstructure. Consequently, maximizing the sensitivity for spectral X-ray dark-field radiography may not be advantageous. Although the sensitivity was not varied in the simulations, it can be assumed that the differentiation of fibrosis and emphysema in spectral XDF imaging is generally feasible for sensitivities where the corresponding correlation length is smaller than the alveoli.

In addition to the sensitivity, the measured signal ratio q_{meas} strongly depends on the projected thickness of lung tissue. The visual comparison of CT images of a human thorax and the cross-section of the FORBILD phantom suggests that the projected lung tissue thickness does not decrease as much toward the edges as in the phantom. For this reason,

the measured signal ratio may be more homogeneous in experiments than in the simulation.

Both beam-hardening by attenuation and visibility hardening by strong scattering influence the dark-field signal. The low-energy bin is particularly susceptible to beam-hardening induced dark-field [17]. The influence of beam-hardening is visible in Fig. 4(d) and (i). Beam-hardening increases toward the phantom center in the low energy bin, because the projected thickness of the soft tissue increases. As a result, the corrected signal ratio increases toward the center of the thorax phantom. Correction methods for beam-hardening induced dark-field were previously developed by Pelzer *et al.* [18] and Bevins *et al.* [46], among others.

The energy-dependency of the linear diffusion coefficient leads to a hardening of the visibility spectrum. Low energy photons are scattered more strongly compared to high energy photons. Consequently, the visibility at low energies is lower compared to the high energies. The influence of visibility hardening on the dark-field signal is more pronounced in the low energy bin.

We have applied an empirical correction method to reduce visibility hardening effects in the thorax phantom radiographs. The correction approach is based on the difference between the expected and the measured signal ratio depending on the projected lung thickness and is able to reduce artifacts owing to visibility hardening. Nevertheless, the experimental implementation of this correction method could be difficult, since we used the estimated lung thickness and Δq from the phantom without pathologies (case A) to correct both versions of the phantom (case A and B). This was possible because of the same sample composition and position in both cases. However, this is not feasible for clinical applications, necessitating a different approach.

For example, conventional spectral transmission data could be used to estimate the lung thickness. The calculation of a geometric model of the lung from X-ray projection images using a deep neural network based method was recently presented [47]. Alternatively, the polychromatic effects could be eliminated by a more sophisticated dual-energy XDF material decomposition [39].

The corrected signal ratio q_{cor} is only a qualitative measure of the energy-dependency of the linear diffusion coefficient. The signal ratio q is influenced not only by visibility hardening, but also other polychromatic effects. In numerical simulations a quantitative distortion correction is possible, because the source spectrum, the detector response and the sample composition are known exactly. However, this is usually not the case in experiments and exact measurements of the spectra are challenging. The signal ratio q_{cor}, nevertheless, provides additional information to the conventional XDF image. If one is aware of the artifacts and the behavior of the measured signal ratio as a function of the lung thickness, a correction is not absolutely necessary, since the differentiation between healthy and diseased lung tissue is already possible prior to the visibility hardening correction.

Although CPFE usually exhibits upper lobe emphysema and lower lobe fibrosis, it cannot be excluded that both pathologies overlap in the projected image, which may impede their differentiation. To counteract this problem, the patient could be imaged in lateral view. Because emphysema and fibrosis typically affect larger areas, they can then be differentiated in either one of the views. Furthermore, spectral XDF computed tomography could provide three-dimensional information.

In our simulations, we assumed a phase stepping with full-field gratings, which is not yet realistic with respect to clinical applicability and manufacturing problems. However, the experimental implementation of grating-based XDF imaging with a fringe-scanning approach has already been demonstrated. The upgrade to spectral XDF imaging could be achieved either by using spectral detector systems or by taking two images with different photon spectra. In our calculations of spectral XDF radiographs, we used a photon-counting detector with a field-of-view of 70 cm × 70 cm to ensure a realistic size of the FORBILD thorax phantom. Due to limitations in manufacturing of the semiconductor sensor layer, especially in the case of cadmium telluride, such a large sensor area could not be achieved today. Photon-counting detectors consist of several modules, which so far cannot be arranged arbitrarily. Therefore, a large field-of-view is only possible in one direction. With regard to an interferometer with fringe-scanning in slit geometry, however, this limitation is not problematic.

Another advantage of photon-counting detectors is that the thresholds can be individually adjusted to the image task, which offers a greater flexibility compared to the acquisition with two different photon spectra. For example, the thresholds could be optimized to optimally exploit the differences in the energy-dependency of lung diseases. In addition, the pixel-wise registration between low and high energy measurements with photon-counting detectors is advantageous, because movements of the patient between two separate image acquisitions can cause artifacts.

Alternatively, the scanning approach offers the opportunity to stack two Talbot-Lau interferometers along the scanning direction. Using different filtration for each interferometer could achieve a good spectral separation also with a conventional flat-panel detector with a single measurement. The design energy of each interferometer should match the mean energy of the low energy and high energy spectrum, respectively, to optimize the visibilities.

Closely related to the selected acquisition method is the total scan time. For the fringe-scanning approach, an acquisition time of 40 s was reported [13], which is realistic for clinical applications, but leaves room for improvement.

The chosen simulation parameters of the source and setup were realistic. The pixel size of the detector was large compared to conventional radiography flat-panel detectors, which have a pixel size in the range of 100 μm to 200 μm. This reduced the computational complexity of the simulation. However, the use of detectors with smaller pixel sizes for spectral XDF radiography is possible. For example, the data acquisition could be performed with a conventional radiography detector and the transmission image would have a higher resolution comparable to conventional radiography (due to a magnification above one). Before processing, binning of the raw data (e.g., 3 × 3 binning of a detector with 150 μm pixel size results in a pixel size of 450 μm) could provide sufficient statistics in the dark-field channel at a clinically

relevant dose. The loss of resolution in the dark-field channel is not problematic, because structural lung diseases typically occur over a large area.

The size of the FORBILD thorax phantom was constant for the different simulated cases. However, in clinical practice, the size of the thorax can vary strongly among patients. A larger thickness in beam direction increases the amount of scattered radiation (not due to the micro structure of the alveoli). The impact of Compton scattering was not considered in the simulations. The additional scatter background can decrease the contrast-to-noise ratio of q. Although Compton scattering in XDF imaging is generally reduced by the setup geometry (G_2 acts as an anti-scatter grid and the distance between sample and detector is large), it cannot be ruled out that the contrast-to-noise ratio of q decreases such that the differentiation of fibrosis and emphysema is compromised. Different approaches can be used to ensure a sufficient image quality. For instance, kernel-based scatter corrections, as used in conventional clinical radiography systems, can isolate and remove scatter from the final images [48], [49].

The KAP in our simulations was $0.82 \, \text{Gy·cm}^2$. The KAP for a normal-sized adult human in thorax radiography in posterior-anterior position is about $0.1 \, \text{Gy·cm}^2$, for the abdomen the KAP is at $2.5 \, \text{Gy·cm}^2$ [50]. The comparison suggests that spectral XDF radiography is feasible with clinically compatible dose levels. Although the KAP was higher in our study compared to conventional thorax radiography, it was still less compared to CT, the state-of-the-art imaging method for the diagnosis of CPFE [15]. In view of the clinical applications of the fringe-scanning approach, recent experiments on grating-based X-ray dark-field human chest radiography were able to achieve a mean total effective dose of approximately $0.040 \, \text{mSv}$ with a conventional flat-panel detector [51].

V. Conclusion

We have determined the energy-dependency of the XDF signal for different lung pathologies with both wave-propagation simulations and analytical calculations. Both results were in good agreement and provide information on how the linear diffusion coefficients of structures similar to the lung parenchyma vary with the X-ray energy. This knowledge is important for future spectral XDF imaging techniques, such as dual-energy dark-field material decomposition for diagnostic lung imaging [39].

The forward-model based calculations of spectral XDF radiographs of the thorax phantom showed the possibility to directly differentiate structural changes in the human lung parenchyma, such as fibrosis and emphysema. Despite the discussed limitations, spectral XDF imaging potentially combines several advantages of state-of-the-art diagnostic imaging techniques, such as low dose, fast examination and increased sensitivity compared to conventional chest radiography.

References

[1] Y. Sekine, H. Katsura, E. Koh, K. Hiroshima, and T. Fujisawa, "Early detection of COPD is important for lung cancer surveillance," *Eur. Respiratory J.*, vol. 39, no. 5, pp. 1230–1240, May 2012.

[2] C. H. McCollough, J. T. Bushberg, J. G. Fletcher, and L. J. Eckel, "Answers to common questions about the use and safety of CT scans," *Mayo Clinic Proc.*, vol. 90, no. 10, pp. 1380–1392, Oct. 2015.

[3] M. O. Wielpütz, C. P. Heußel, F. J. F. Herth, and H.-U. Kauczor, "Radiological diagnosis in lung disease: Factoring treatment options into the choice of diagnostic modality," *Deutsches Ärzteblatt Int.*, vol. 111, no. 11, pp. 181–187, 2011.

[4] H. W. Goo and J. M. Goo, "Dual-energy CT: New horizon in medical imaging," *Korean J. Radiol.*, vol. 18, no. 4, p. 555, 2017.

[5] R. Ballabriga *et al.*, "Review of hybrid pixel detector readout ASICs for spectroscopic X-ray imaging," *J. Instrum.*, vol. 11, no. 1, 2017, Art. no. P01007.

[6] B. Ruzsics, H. Lee, P. Zwerner, M. Gebregziabher, P. Costello, and U. Schoepf, "Dual-energy CT of the heart for diagnosing coronary artery stenosis and myocardial ischemia-initial experience," *Eur. Radiol.*, vol. 18, pp. 2414–2424, Jun. 2008.

[7] L.-J. Zhang *et al.*, "Liver virtual non-enhanced CT with dual-source, dual-energy CT: A preliminary study," *Eur. Radiol.*, vol. 20, no. 9, pp. 2257–2264, Sep. 2010.

[8] S. Kuchenbecker, S. Faby, S. Sawall, M. Lell, and M. Kachelrieß, "Dual energy CT: How well can pseudo-monochromatic imaging reduce metal artifacts?" *Med. Phys.*, vol. 42, no. 2, pp. 1023–1036, Jan. 2015.

[9] F. Pfeiffer *et al.*, "Hard-X-ray dark-field imaging using a grating interferometer," *Nature Mater.*, vol. 7, no. 2, pp. 134–137, 2008.

[10] S. Schleede *et al.*, "Emphysema diagnosis using X-ray dark-field imaging at a laser-driven compact synchrotron light source," *Proc. Nat. Acad. Sci. USA*, vol. 109, no. 44, pp. 17880–17885, 2012.

[11] K. Hellbach *et al.*, "*In vivo* dark-field radiography for early diagnosis and staging of pulmonary emphysema," *Investigative Radiol.*, vol. 50, no. 7, pp. 430–435, Jul. 2015.

[12] A. Yaroshenko *et al.*, "Improved *in vivo* assessment of pulmonary fibrosis in mice using X-ray dark-field radiography," *Sci. Rep.*, vol. 5, no. 1, p. 17492, Dec. 2015.

[13] L. B. Gromann *et al.*, "*In-vivo* X-ray dark-field chest radiography of a pig," *Sci. Rep.*, vol. 7, no. 1, p. 4807, Dec. 2017.

[14] K. Willer *et al.*, "X-ray dark-field imaging of the human lung— A feasibility study on a deceased body," *PLoS ONE*, vol. 13, no. 9, 2018, Art. no. e0204565.

[15] M. D. Jankowich and S. I. S. Rounds, "Combined pulmonary fibrosis and emphysema syndrome: A review," *Chest*, vol. 141, pp. 222–231, Jan. 2012.

[16] K. Taphorn, F. D. Marco, J. Andrejewski, T. Sellerer, F. Pfeiffer, and J. Herzen, "Grating-based spectral X-ray dark-field imaging for correlation with structural size measures," *Sci. Rep.*, vol. 10, no. 1, p. 13195, Dec. 2020.

[17] W. Yashiro, P. Vagovič, and A. Momose, "Effect of beam hardening on a visibility-contrast image obtained by X-ray grating interferometry," *Opt. Exp.*, vol. 23, no. 18, pp. 23462–23471, 2015.

[18] G. Pelzer *et al.*, "A beam hardening and dispersion correction for X-ray dark-field radiography," *Med. Phys.*, vol. 43, no. 6, pp. 2774–2779, May 2016.

[19] F. De Marco *et al.*, "X-ray dark-field signal reduction due to hardening of the visibility spectrum," 2020, *arXiv:2011.03542*. [Online]. Available: http://arxiv.org/abs/2011.03542

[20] *FORBILD Phantoms*. Accessed: May 29, 2020. [Online]. Available: http://www.imp.uni-erlangen.de/phantoms/

[21] F. Pfeiffer, T. Weitkamp, O. Bunk, and C. David, "Phase retrieval and differential phase-contrast imaging with low-brilliance X-ray sources," *Nature Phys.*, vol. 2, no. 4, pp. 258–261, Apr. 2006.

[22] D. M. Paganin, *Coherent X-ray Optics*. Oxford, U.K.: Oxford Univ. Press, 2006.

[23] P. Willmott, *An Introduction to Synchrotron Radiation: Techniques and Applications*, 1st ed. Hoboken, NJ, USA: Wiley, 2013.

[24] F. Prade, A. Yaroshenko, J. Herzen, and F. Pfeiffer, "Short-range order in mesoscale systems probed by X-ray grating interferometry," *EPL Europhys. Lett.*, vol. 112, no. 6, p. 68002, Dec. 2015.

[25] M. Strobl, "General solution for quantitative dark-field contrast imaging with grating interferometers," *Sci. Rep.*, vol. 4, no. 1, p. 7243, May 2015.

[26] W. Yashiro, Y. Terui, K. Kawabata, and A. Momose, "On the origin of visibility contrast in X-ray talbot interferometry," *Opt. Exp.*, vol. 18, no. 16, pp. 16890–16901, 2010.

[27] R. Andersson, L. F. van Heijkamp, I. M. D. Schepper, and W. G. Bouwman, "Analysis of spin-echo small-angle neutron scattering measurements," *J. Appl. Crystallogr.*, vol. 41, no. 5, pp. 868–885, Oct. 2008.

[28] V. Garanzha, L. Kamenski, and H. Si, "Numerical geometry, grid generation and scientific computing," in *Proc. 9th Int. Conf. NUMGRID*, 2019, pp. 45–60.

[29] S. V. Hooff *et al.*, "Innovative methodology to mimic lung parenchyma based on Voronoi models: Application to 3d-printed anthropomorphic CT image quality phantoms," presented at the 105th Sci. Assem. Annu. Meeting, Chicago IL, USA, Dec. 2019. Accessed: Apr. 23, 2020. [Online]. Available: http://archive.rsna.org/2019/19006024.html

[30] J. Koketsu *et al.*, "3D-printable lung phantom for distal falloff verification of proton Bragg peak," *J. Appl. Clin. Med. Phys.*, vol. 20, no. 9, pp. 86–94, Sep. 2019.

[31] J. E. McDonough, L. Knudsen, A. C. Wright, W. M. Elliott, M. Ochs, and J. C. Hogg, "Regional differences in alveolar density in the human lung are related to lung height," *J. Appl. Physiol.*, vol. 118, no. 11, pp. 1429–1434, Jun. 2015.

[32] F. Y. Shih, *Image Processing and Mathematical Morphology: Fundamentals and Applications*. Boca Raton, FL, USA: CRC Press, 2009.

[33] H. Matthys and W. Seeger, Eds., *Klinische Pneumologie*, 4th ed. Heidelberg, Germany: Springer, 2008.

[34] L. Knudsen, E. R. Weibel, H. J. G. Gundersen, F. V. Weinstein, and M. Ochs, "Assessment of air space size characteristics by intercept (chord) measurement: An accurate and efficient stereological approach," *J. Appl. Physiol.*, vol. 108, no. 2, pp. 412–421, Feb. 2010.

[35] R. Nowotny. *XMuDat: Photon Attenuation Data on PC*. Accessed: Nov. 20, 2020. [Online]. Available: https://www-nds.iaea.org/publications/iaea-nds/iaea-nds-0195.htm

[36] J. M. Boone and A. E. Chavez, "Comparison of X-ray cross sections for diagnostic and therapeutic medical physics," *Med. Phys.*, vol. 23, no. 12, pp. 1997–2005, Dec. 1996.

[37] J. Wolf *et al.*, "Fast one-dimensional wave-front propagation for X-ray differential phase-contrast imaging," *Biomed. Opt. Exp.*, vol. 5, no. 10, pp. 3739–3747, 2014.

[38] A. Malecki, G. Potdevin, and F. Pfeiffer, "Quantitative wave-optical numerical analysis of the dark-field signal in grating-based X-ray interferometry," *EPL Europhys. Lett.*, vol. 99, no. 4, p. 48001, Aug. 2012.

[39] T. Sellerer, K. Mechlem, R. Tang, K. Taphorn, F. Pfeiffer, and J. Herzen, "Dual-energy X-ray dark-field material decomposition," 2020, *arXiv:2007.00585*. [Online]. Available: http://arxiv.org/abs/2007.00585

[40] K. Mechlem, T. Sellerer, M. Viermetz, J. Herzen, and F. Pfeiffer, "Spectral differential phase contrast X-ray radiography," *IEEE Trans. Med. Imag.*, vol. 39, no. 3, pp. 578–587, Mar. 2020.

[41] J. P. Schlomka *et al.*, "Experimental feasibility of multi-energy photon-counting K-edge imaging in pre-clinical computed tomography," *Phys. Med. Biol.*, vol. 53, no. 15, pp. 4031–4047, Aug. 2008.

[42] C. Kottler, V. Revol, R. Kaufmann, and C. Urban, "Dual energy phase contrast X-ray imaging with Talbot-Lau interferometer," *J. Appl. Phys.*, vol. 108, no. 11, 2010, Art. no. 114906.

[43] W. Schlegel and J. Bille, *Medizinische Physik 2: Medizinische Strahlenphysik*. Berlin, Germany: Springer-Verlag, 2002.

[44] J. C. Woods *et al.*, "Hyperpolarized ^{3}He diffusion MRI and histology in pulmonary emphysema," *Magn. Reson. Med.*, vol. 56, no. 6, pp. 1293–1300, 2006.

[45] E. K. Verbeken, M. Cauberghs, J. M. Lauweryns, and K. P. Van de Woestijne, "Structure and function in fibrosing alveolitis," *J. Appl. Physiol.*, vol. 76, no. 2, pp. 731–742, Feb. 1994.

[46] N. Bevins, K. Li, J. Zambelli, and G.-H. Chen, "Type II beam hardening artifacts in phase contrast imaging," *Proc. SPIE*, vol. 8668, pp. 308–313, Mar. 2013.

[47] Y. Wang, Z. Zhong, and J. Hua, "DeepOrganNet: On-the-fly reconstruction and visualization of 3D / 4D lung models from single-view projections by deep deformation network," *IEEE Trans. Vis. Comput. Graphics*, vol. 26, no. 1, pp. 960–970, Jan. 2020.

[48] L. A. Love and R. A. Kruger, "Scatter estimation for a digital radiographic system using convolution filtering," *Med. Phys.*, vol. 14, no. 2, pp. 178–185, Mar. 1987.

[49] M. Sun and J. M. Star-Lack, "Improved scatter correction using adaptive scatter kernel superposition," *Phys. Med. Biol.*, vol. 55, no. 22, pp. 6695–6720, Nov. 2010.

[50] W. Huda, "Kerma-area product in diagnostic radiology," *Amer. J. Roentgenol.*, vol. 203, no. 6, pp. W565–W569, Dec. 2014.

[51] M. Frank *et al.*, "Dosimetry for combined dark-field and attenuation chest X-ray imaging on patients," presented at the 105th Sci. Assem. Annu. Meeting, Chicago IL, USA, Dec. 2019. Accessed Apr. 23, 2020. [Online]. Available: http://archive.rsna.org/2019/19003942.html